

Article

Determination of the Stability of High-Steep Slopes by Global Navigation Satellite System (GNSS) Real-Time Monitoring in Long Wall Mining

Xugang Lian ^{1,*}, Zoujun Li ¹, Hongyan Yuan ², Haifeng Hu ¹, Yinfei Cai ¹ and Xiaoyu Liu ¹

¹ Department of Surveying and Mapping, Taiyuan University of Technology, Taiyuan 030024, China; lizoujun0560@link.tyut.edu.cn (Z.L.); tyhhf65@163.com (H.H.); caiyinfei@tyut.edu.cn (Y.C.); liuxiaoyu0586@link.tyut.edu.cn (X.L.)

² Department of Municipal Engineering, Shanxi Architectural College, Jinzhong 030619, China; yhy84127@sina.com

* Correspondence: lianxugang@tyut.edu.cn

Received: 7 February 2020; Accepted: 9 March 2020; Published: 12 March 2020



Abstract: Surface movement and deformation induced by underground coal mining causes slopes to collapse. Global Navigation Satellite System (GNSS) real-time monitoring can provide early warnings and prevent disasters. A stability analysis of high-steep slopes was conducted in a long wall mine in China, and a GNSS real-time monitoring system was established. The moving velocity and displacement at the monitoring points were an integrated response to the influencing factors of mining, topography, and rainfall. Underground mining provided a continuous external driving force for slope movement, the steep terrain provided sufficient slip conditions in the slope direction, and rainfall had an acceleration effect on slope movement. The non-uniform deformation, displacement field, and time series images of the slope body revealed that ground failure was concentrated in the area of non-uniform deformation. The non-uniform deformation was concentrated ahead of the working face, the speed of deformation behind the working face was reduced, the instability of the slope body was increased, and the movement of the top of the slope was larger than at the foot. The high-steep slope stability in the mine was influenced by the starting deformation (low stability), iso-accelerated deformation (increased stability), deformation deceleration (reduced stability), and deformation remaining unchanged (improved stability).

Keywords: GNSS monitoring system; long wall mining; dynamic deformation; high-steep slope; stability

1. Introduction

Natural disasters, such as earthquakes, tsunamis, volcanoes, landslides, ground subsidence, debris flows, and pit collapses, can be extremely harmful to human societies. In terms of scale, earthquakes and tsunamis are violent and dangerous and pose a great threat to human beings, but due to their quantity, landslides are the second most serious threat. Approximately 8000 human casualties can be attributed to landslides each year, with direct economic losses exceeding \$1 billion. In China alone, 640,000 km² land is covered by loess [1], which is loose, porous, collapsible, and has a weak load-bearing capacity, resulting in a risk of landslides, debris flows, and other disasters. In addition, landslides have become more frequent due to earthquakes, and increases and decreases in the groundwater level, rainfall, mining, and other factors. For example, the Wenchuan earthquake occurred on 12 May 2008 [2], and caused a number of large landslides, resulting in heavy human casualties. The Three Gorges Dam is an internationally renowned engineering project because of its high water storage capacity, which has resulted in changes in the groundwater level. Changes in rainfall amounts, groundwater levels, and weak sliding surfaces have increased the occurrence of landslides [3].

The occurrence of geological disasters such as landslides often leads to immense losses to human societies, and have; therefore, attracted much attention from governments worldwide, as well as experts and researchers in related fields. Many studies have been conducted on the early identification, inducement, characteristics, classification, prevention, and control of landslides, including stability analyses, spatial and temporal predictions, and early warning and forecasting. Several studies have used satellite remote sensing images, interferometric radar (InSAR), laser ranging (LIDAR), unmanned aerial vehicles (UAVs) low-altitude remote sensing images, field investigations, and other methods to identify the distribution and slope features of landslides [4–7]. Other studies have applied finite element, discrete element, and other numerical simulation methods as well as material simulation experiments to conduct stress-strain analyses and determine the causes of instability at the time of slope failure [8–10]. To better apply their results to engineering practice, researchers have classified landslides into peristaltic landslides [11], rainfall induced landslides [12], mining landslides, and seismic landslides [13]. Because theoretical studies of landslides have been conducted in China, the measures and methods used to respond to landslides are improving, and the state's funds allocated for disaster prevention and control have increased over time. However, China is unable to comprehensively control all landslides and potentially unstable slopes under the present conditions, and it is therefore necessary to ensure the prediction and early warning of landslide disasters and reduce the losses associated with them. Previous attempts to develop slope failure early warning systems have mainly been conducted through field surveys and investigations, studies of stratigraphic geomorphology to statistically analyze the possibility of a landslide occurrence, or through the installation of observation stations, displacement meters, and depth meters to obtain monitoring data. This has been followed by the application of a variety of predictive models, such as the grey model (GM), polynomial regression model, machine forest model, logical regression model, strength reduction method, and back propagation (BP) neural network [13–16]. In recent years, with the expansion in the application of geographic information systems (GIS) and the maturity of satellite differential positioning technology, Global Navigation Satellite System (GNSS) real-time monitoring systems have made a breakthrough in the field of landslide early warning and prediction [17,18]. The intensive study of landslides has achieved many useful outcomes, but there are still some problems with the application of GNSS monitoring systems for use on high-steep slopes in coal mining subsidence areas, and there has been insufficient research on the specific influences of high-steep slopes in mines, the surrounding topography, rainfall, and other associated parameters.

GNSS is used to monitor the crustal deformation of the post-earthquake, such as a detailed crustal deformation model using three-component GNSS data in 2000–2010 was construct for the 2016 Kumamoto earthquakes in central Kyushu, Japan [19], and also used for other seismic analyses, such as the Izmit earthquake [20] in the north-west of Turkey on 17 August 1999, Wenchuan earthquake [21] on 12 May 2008 and Jiuzhaigou earthquake [22] on 8 August 2017 in Sichuan province, China. GNSS monitoring results of crustal deformation are often applied to earthquake prediction, for example, 31 GNSS stations from the Crustal Movement Observation Network of China (CMONOC) were used to study regional crustal deformation characteristics in Xinjiang, China [23]. Block modeling of crustal deformation in Tierra del Fuego from GNSS velocities of 41 sites was established [24]. A regional GNSS network consisting of 202 permanent GNSS stations established to study the recent crustal strain deformation in the Ukrainian territory [25]. A right-lateral shear zone in the San-in region, southwest Japan, has been proposed by previous geological and seismological studies, and was proved using GNSS velocity data [26]. Crustal deformation across the Southern Patagonian Icefield was observed by 43 GNSS sites [27]. Small crustal deformation caused by slow slip events in southwest Japan was detected using GNSS and tremor data [28]. GNSS also is applied in frost heave deformation [29,30], volcanic deformation [31,32], mining subsidence [33], bridge deformation [34,35], and dam deformation [36,37], and so on. The advantages of GNSS monitoring are (a) allow sampling at any time interval, (b) remote and severe weather data collection can be achieved, (c) avoid human errors caused by manual readings and records, (d) 24 h a day for continuous monitoring. The disadvantages are single point data, and the high cost to form lines or networks.

In the long wall coal mining method, the mining area is divided along the working direction into several strip-shaped sections. Along the coal seam at the lower elevation level there is a roadway for coal transport, while in the upper elevation level there is a return air roadway. The first cut of the coal mining face is arranged between two sections of the roadway, along the dip direction of the coal seam. Coal mining advances along the direction of the coal seam. After underground coal mining, the rock formation around the mining space loses its support and gradually moves, bends, and deforms into the goaf. This process gradually extends from the slope outwards and upward to the surface as the mining face continues to push forward, causing the surface to sink, and forming a subsidence basin. The movement of the overlying rocks and surface deformation is inevitable as new equilibrium conditions for mine failure are formed due to changes in the original stress state of the rocks.

In this study, a GNSS real-time monitoring system was used for the first time to assess the dynamic deformation of the overlying rock mass and the high-steep slope in long wall mining. The dynamic changes of the overlying rock layer and slope body were determined based on the moving velocity and material displacement at the monitoring point. The study demonstrated the applicability of a GNSS real-time monitoring and warning system in a high-steep slope, and proposed a new way to assess the evolution of dynamic deformation and stability of a high-steep slope under mining conditions.

2. Overview of the Study Area

Figure 1 shows the position of a landslide above Luhuvillage in Shanxi Province, China. The region around the village is a mining area, with the mine in panel A having a depth of 470 m, thickness of 6.5 m, width of 200 m, and length of 1200 m; and the mine in panel B had a depth of 390 m, thickness of 2.5 m, width of 220 m, and length 1162 m. The area investigated had a largely undulating terrain, with steep slopes. The vegetation in this area is mainly shrubs, and the area has a temperate continental climate, with annual rainfall of less than 600 mm, which is mainly concentrated in July, August, and September. The loess layer in this area is very thin and the bedrock is exposed. The strata are North China continental facies, with Carboniferous (C), Permian (P), and Quaternary (Q) outcrops. The total thickness of the coal series strata is 220–260 m.

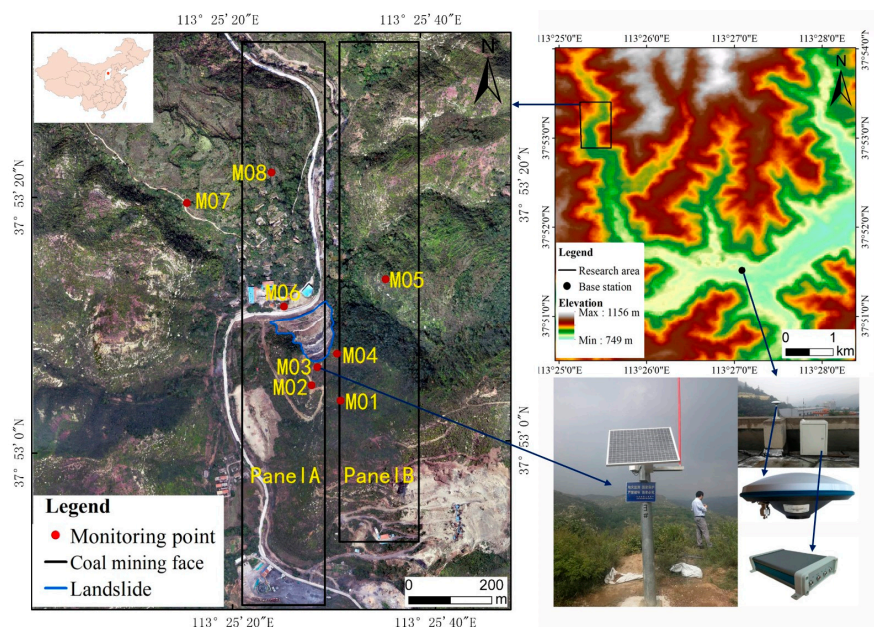


Figure 1. Overview of the study area and distribution of Global Navigation Satellite System (GNSS) monitoring points.

The initial landslide occurred in February 2017 and now forms a high-steep slope, with a height of about 100 m, an area of 11,563.7 m², and slope of more than 45°. There is a strong potential for mining

activities to initiate secondary landslides. There is a road and river around the landslide. The river flows to the southeast and is seasonal, with water only in the rainy season. The valley is about 150 m wide, the valley floor elevation is 825–830 m, the change of gradient is about 15%, the two sides of the valley are mostly wasteland, and some bedrock is exposed. There are a small number of terraces on the west side of the valley. Luhu village is located near the road and the Luhu River, on the northwest side of the slope body, and is close to the high-steep slope.

3. Monitoring Methods and Principles

3.1. Composition of the GNSS Monitoring System

Based on the spatial relationship between the slope body and the two panels, a GNSS real-time monitoring system was established at the landslide above Luhu village. The system consisted of eight monitoring points and a base station, and their location is shown in Figure 1, where the monitoring points M01–M04 were located at the top of the high-steep slope, M06 was located at the bottom of the slope, and M07 and M08 were located at the south of the panel A, while M05 was located at the center of the panel B, which was also at the top of the other slope. At each point, the foundation pit of $60 \times 60 \times 60$ cm was excavated on the ground, then the connecting steel bar was embedded, the concrete was poured to form the foundation, and the monitoring station can be fixed to the foundation by screws to be stable. The height of each station was 2.3 m, which ensured it can receive enough strong signals from satellites. To ensure the stability of the base station, it was arranged at a distance of about 4 km from the mining area to form the local area network (LAN) differential positioning mode. The system consisted of a monitoring module, power supply module, video monitoring module, and rainfall monitoring module, and its detailed composition is shown in Figure 2. The monitoring module consisted of a GNSS receiver, antenna, general packet radio service (GPRS) data transmission module, and an early warning and alarm module. The system was solar powered and was equipped with a battery storage system, which ensured continuous operation for five days as well as operation on rainy days. The system could obtain real-time monitoring data, and the accuracy of a 1 h static observation solution could reach the mm level. The precision of GNSS PPP (precise point positioning), RTK (real-time kinematic) and static baseline positioning based on landslide monitoring are better than 6 cm, 6 and 3 mm, respectively [38], which was verified a landslide monitoring.

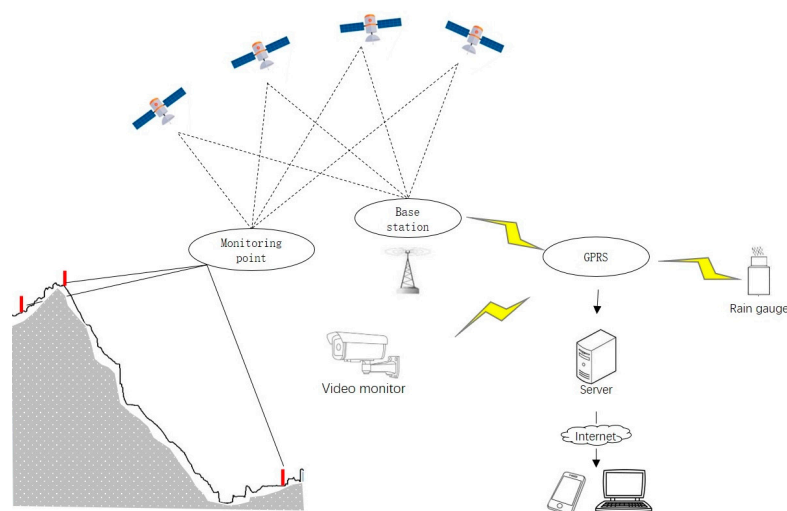


Figure 2. GNSS real-time monitoring system for the Luhu village slope.

3.2. Operating Principle and Data Acquisition of the Monitoring System

The GNSS monitoring system used its positioning function to determine the location of monitoring points. Since the focused point of this study was relative displacement, and the requirement for absolute

coordinate accuracy was low, the initial coordinate system was determined by the default Universal Transverse Mercator (UTM) projection system. GNSS receiver model was LPR2000 series, which has built-in UB380 board module to receive signals from BDS, GPS, GLONASS satellite, shown in Table 1; built-in low-power radio to support differential data transmission between stations; equipped with GPRS-4G module to support remote interface control and remote data transmission to realize remote monitoring ability of measuring points. The HC Monitor software was used for GNSS data processing, it has the advantages of using the nonlinear Kalman filtering of double-differential and three-differential algorithms, the improved ionospheric correction model, and supporting the multi-reference station solution and real-time independent baseline network adjustment. The horizontal accuracy was better than 3 mm and the elevation was 5 mm. Calculating coordinates at a speed of once per 5 s, and achieve millimeter level accuracy; the solution data was transmitted to the server at a speed of once per 5 s through GPRS-4G, the coordinates and the displacement, speed and acceleration calculations of the monitoring points can be read and downloaded at the port of the web page version of the ground disaster monitoring system, which also sent the relevant alarm information to the user by detecting whether the deformation data was greater than the warning value. Similarly, the rainfall sensor and the video sensor were used to obtain real-time rainfall information and a video of the slope, respectively. The data were transmitted in the same way as the GNSS monitoring module data. The end user could obtain deformation and rainfall information, as well as other data through the internet and via mobile phone. The LAN differential location data of the monitoring system was obtained for a 90-day period in this study, with an acquisition frequency of once a day.

Table 1. The parameters of UB380 board module.

Signal	Time Precision	Static Surveying Accuracy	Differential Protocol
BDS: B1/B2/B3 GPS: L1/L2/L5 GLONASS: L1/L2	20 ns	Horizontal: 2.5 mm + 1 ppm; Elevation: 5.0 mm + 1 ppm	RTCM 2.x/3.x, CMR

4. Results and Discussion

4.1. Slope Movement Velocity Analysis

In the process of underground coal seam mining, the overlying strata will experience subsidence, tilt, horizontal movement, horizontal strain, and other deformations, which often lead to the destruction of surface buildings, slope slippage, and surface cracks. In this study, the dynamic deformation of slope and the active state of the overlying strata were assessed by setting real-time GNSS monitoring points. According to the X, Y, and Z coordinates of each monitoring point, the displacement and moving velocity of the monitoring points in 3D space were calculated and the factors influencing the deformation of the slope body in the mining area were analyzed.

According to Figures 3 and 4:

(1) After operating the monitoring system, the working face in panel A advanced 10 m beyond monitoring point M01, and its velocity in each direction was relatively small (within 20 mm/d) and stable. After 50 days of monitoring, because the working face in panel B was close to M01 (about 100 m), the influence of mining ahead of the monitoring point increased its X and Z directional movement. When the distance between the working face and M01 was more than 386 m, the V_z of the monitoring point was slightly larger than the V_x and V_y .

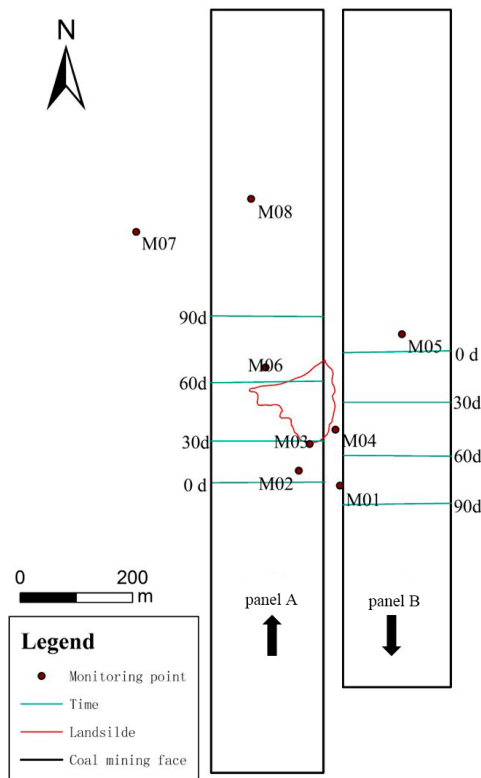


Figure 3. Map of the advancing work face of the mining activity in panels A and B.

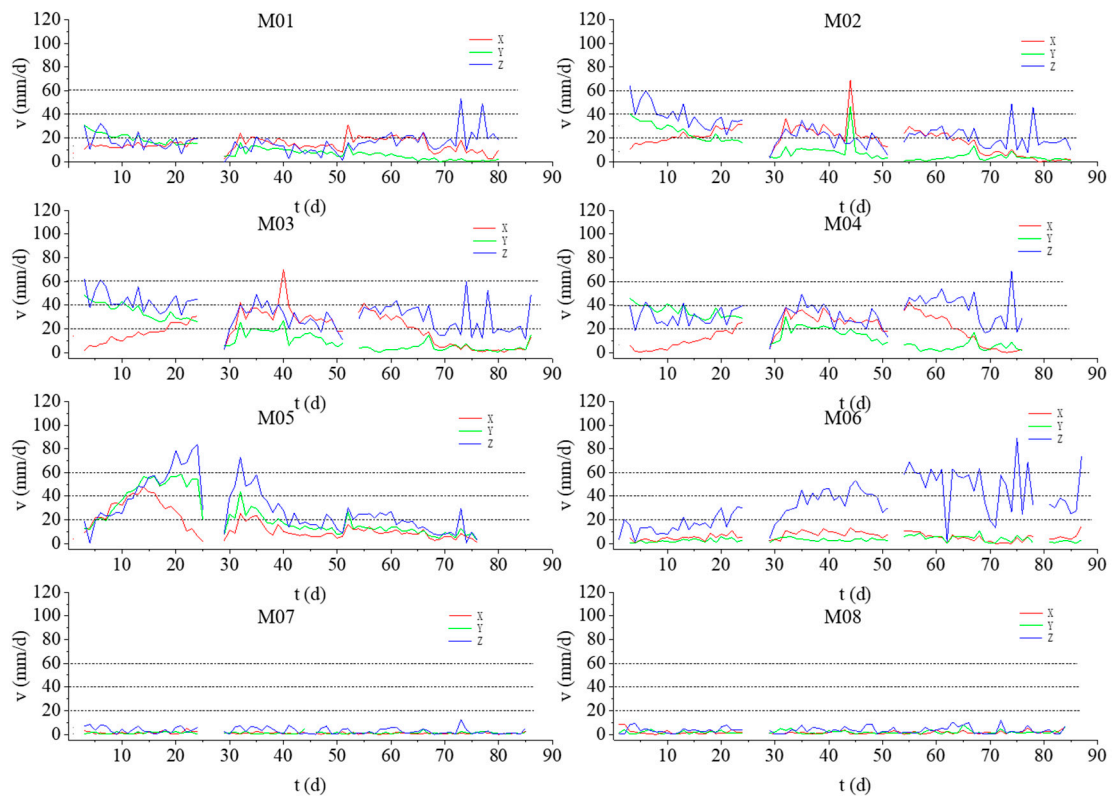


Figure 4. One-dimensional moving velocity curves.

(2) When the working face in panel A passed through M02, the V_y and V_z at the monitoring point gradually decreased, and V_x initially increased and then decreased. As the distance from the working face to M02 gradually increased, the V_x became larger than the V_y and V_z (i.e., the movement in the X direction was more active because M02 was located at the top of the slope), and the disturbance in the downhill direction (X direction) of the slope was greater than the disturbance in the other directions. The velocity in the three directions then became stable at about 20 mm/d. Similarly to at M01, V_z was slightly larger than V_x and V_y when the distance between the working face and M02 exceeded 349 m. The velocity curve at this point increased suddenly at 43 days, especially for V_x and V_y , which was caused by the continuous rainfall shown in Figure 5.

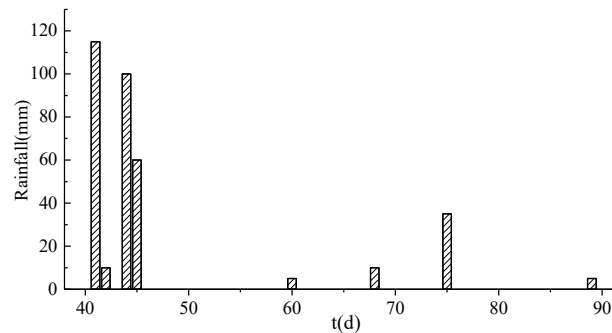


Figure 5. Rainfall statistics in the slope area.

(3) The movement velocity at M03 and M02 was very similar. After monitoring started, V_y and V_z at M03 gradually decreased and eventually stabilized at 30–40 mm/d, while V_x initially increased and then decreased, before becoming more active. Because M03 was located on the shoulder of the landslide slope, the moving velocity at M03 was higher than at M02. When the distance between the working face and M03 in panel A was approximately 300 m, V_x and V_y were synchronized, and V_z became slightly larger. After 67 days of monitoring, all recorded velocities were less than 20 mm/d.

(4) At M04, V_x initially increased and then decreased, V_z increased to around 30 mm/d, and V_y decreased to 20 mm/d. When the distance between the working face and M04 was large, V_x and V_y were synchronous and V_z increased slightly, but all were less than 20 mm/d. Because M04 was located at the outer boundary of panel A, its velocity was less than M03, but its location was close to the downhill direction of the slope body, and therefore it was still larger in the X and Z directions.

(5) At M06, which was located in the middle of panel A close to the bottom of the slope, V_x and V_y were very low (10 mm/d) and the plane movement was small. As the distance between the working face and M06 increased, V_z gradually increased and then decreased, and the vertical direction was severely affected by the mining activity.

(6) The working face in panel A did not pass through M07 and M08 and the displacement velocity at these monitoring points was less than 20 mm/d, and remained in a stable state.

(7) Monitoring point M05 was located on the ground in a position corresponding to the center of panel B. As the working face in panel B moved gradually closer to and away from M05, the displacement velocity first increased and then decreased, and finally remained around 20 mm/d. From the velocity curve, $V_x < V_y < V_z$, and the maximum moving velocity in the plane occurred earlier in the direction in which the land was sinking.

The results could be summarized as follows. (1) The change in the speed of ground movement at the monitoring points was mainly affected by factors such as mining, topography (elevation, slope, and slope direction), and rainfall. When the speed of ground movement at the monitoring point was only slightly affected by mining, the velocity was within 20 mm/d. At this time, although the overlying rock formation was active, the ground stability was acceptable. (2) Because the position of the monitoring points in the two panels and the corresponding terrain were different, the magnitude of the speed of ground movement in the same direction and the time required to achieve stability in the two panels

were different. (3) Under the influence of rainfall, the moving velocity suddenly increased. Although the duration of the increase was short, continuous rainfall over a short period of time resulted in a large disturbance to the stability of the slope body.

4.2. Slope Displacement Analysis

4.2.1. Displacement Analysis

The goaf formed by underground coal mining causes the overlying strata and ground to be deformed. To determine how mining subsidence proceeds and assess the active state of the ground, ground movement observation stations are usually established in the main sections of coal mining areas, and the frequency of monitoring is usually once a month. In this study, the GNSS real-time monitoring system used the X, Y, and Z coordinates of the monitoring points to calculate the moving trajectory of each point once a day. The influence of mining, rainfall, and terrain factors on the moving trajectory was analyzed.

Figure 6 shows that with the advance of the working face, the ground displacement constantly increased at each monitoring point.

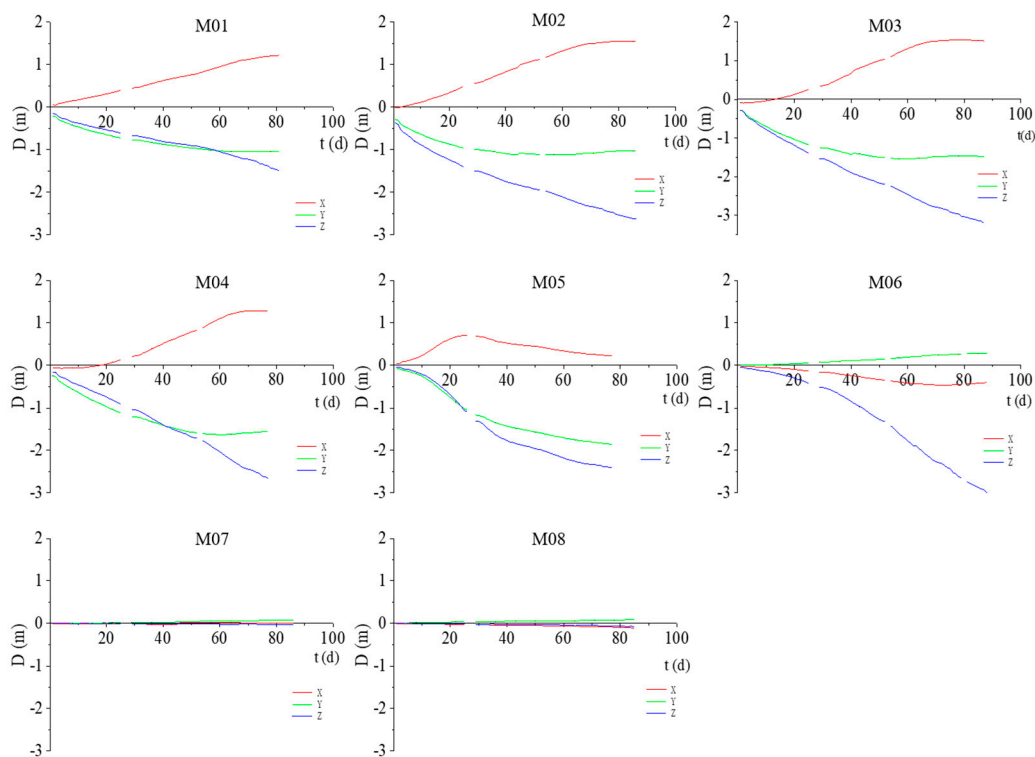


Figure 6. Ground displacement curves at the monitoring points.

(1) X-direction displacement. During the advance of the working face, the moving direction at the monitoring points in the initial stage was the opposite of that of the advancing working face. When the working face crossed the monitoring point, the moving direction at the monitoring points was the same as that of the advancing working face. Because the moving direction was consistent with the downhill direction of the slope body, the slope body slip increased the cumulative displacement of the monitoring points. Figure 7 shows the slope body profile with the advance of the working face.

(2) Y-direction displacement. With the advance of the working face, the monitoring points all moved toward the center of the goaf. When the working face was far from a monitoring point, the horizontal displacement of the monitoring point had a tendency to remain unchanged or to move back to its original position.

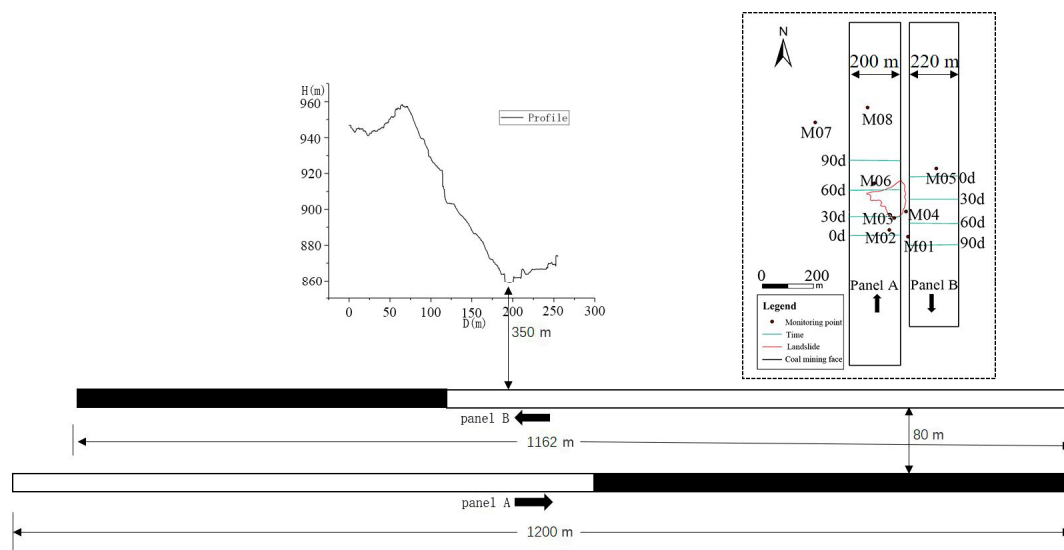


Figure 7. The relationship between the relative position of the slope body and the coal mining activity in both panels.

(3) Z-direction displacement. With the advance of the working face, the magnitude of sinking constantly increased, except at M07 and M08, which were located far from the working face. The closer the monitoring points were to the center of the coal mining activity, the greater the subsidence.

A comparative analysis of the horizontal displacement of the ground at each monitoring point was conducted. The similarities and differences of the moving trends at each monitoring point were related to the topographic conditions at the location of the monitoring point and its ground position above the working face. Monitoring site M06 was located at the bottom of the slope, while M02, M03, M04, and M05 were located at the top of the slope. Because of the poor ground stability at the top of the slope, the horizontal movement at M06 was less than that at M02, M03, M04, and M05. This difference was particularly noticeable on the west side of M05, which was the downward direction of the slope, resulting in an increase in the negative movement of the monitoring point toward the Y-axis. When the working face was far from the monitoring point, the horizontal movement of the monitoring point was reduced, and the movement was dominated by subsidence.

Figure 8 shows the surface movement in the mining process. The horizontal moving track curve of the monitoring point reflects the difference in the moving value at the monitoring point and the trend in different regions over the same time period.

(1) Due to coal mining in panels A and B, the movement trend of monitoring points M01–M04 was the same, but the magnitude of movement was different. The largest movement in the X direction was observed at M02 and M03, while the largest movement in the Y direction was observed at M04. As shown in Figure 1, the X direction of M02 and M03 and the Y direction of M04 were close to the downhill direction of the slope body, and the topographic slope had a large influence on the displacement; therefore, they had large moving values.

(2) In contrast, M06 was located at ground level in the center of panel A. The horizontal movement in the Y-direction is very small and the movement in the X-direction was the opposite of the other monitoring points.

(3) Monitoring point M05 was located at ground level in the center of panel B. The horizontal movement in the strike direction of the working face initially increased and then decreased, while the horizontal movement in the dip direction of the working face increased continuously because it was near the downhill direction of the slope body. For the monitoring points that were less affected by the topography (e.g., M01–M04), as the working face advanced in the X direction, the monitoring points had a tendency to move toward the initial position. In the Y direction, the monitoring points always moved to the center of the working face.

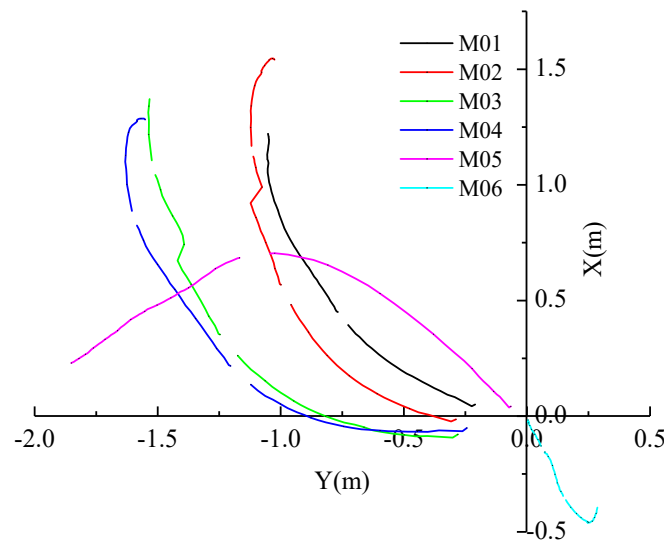


Figure 8. The track of the horizontal movement of the monitoring points.

(4) There was a non-uniform movement of monitoring points with the same horizontal movement trend, but different amounts and directions of movement. There was also non-uniform movement of monitoring points with different horizontal movement trends. These two important factors could cause damage to the mountainside, with the damage due to the surface deformation formed by the latter being greater than that due to the former.

Surface points were affected by coal mining in a complex temporal and spatial process, according to the X-Z section of the monitoring point moving trajectory, as shown in Figure 9.

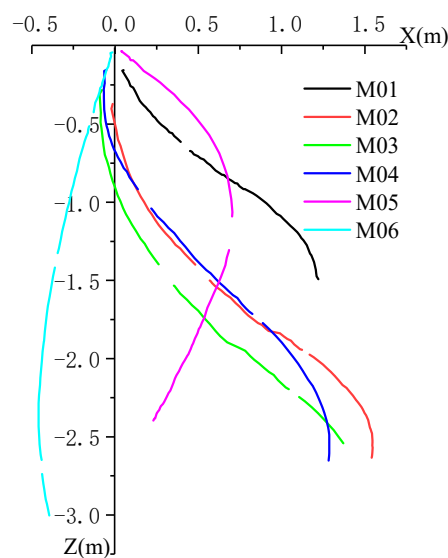


Figure 9. The X-Z profile movement trajectory at the monitoring points.

(1) The ground movements at M02, M03, M04, and M06 in the Z direction were large and were affected by the mining activity in panel A. Monitoring point M01 experienced less subsidence because of the relatively short monitoring time. Larger surface subsidence values were recorded closer to the center of the panel. Monitoring point M05 was mainly affected by the coal mining in panel B. Because the mining thickness in panel B was small, there was less subsidence at this monitoring point than at other locations.

(2) The horizontal movements in the X direction at M02, M03, and M04 were larger than those at other monitoring points, and were mainly affected by the downhill direction of the slope body. When the working face passed over these points it was affected by the topography, with little backward movement in the X direction (i.e., moving to the initial position). The backward movement in the X direction was largest at M05, with M06 also showing a trend of backward movement.

(3) The backward movement of the monitoring points in the X direction is a phenomenon of surface movement caused by the influence of movement ahead and behind a surface point during the passage of the working face. This was clearly observed at M05 and M06, but was limited to varying degrees by the topography at the other monitoring points.

4.2.2. Influence of Mining, Terrain Conditions, and Rainfall on Slope Movement

By analyzing the X, Y, and Z displacement, X–Y plane trajectory, and X–Z profile trajectory of the monitoring points in the study area, we found that:

(1) The influence of mining was the main factor continuously driving the overburden and surface movement as the working face advanced, and the direction of ground movement was determined by the position of the advancing working face. This represented the main driving force for the formation of a slope body slip.

(2) The influence of the terrain conditions on the ground displacement was mainly reflected in an increase in the displacement value in a certain direction, and the monitoring points were greatly affected by the topography in the downhill direction of the slope body. This provided sufficient conditions for a landslide to occur.

(3) The effect of rainfall on the movement and moving velocity of the ground at the monitoring points was periodic, and the formation of a sliding surface of the slope body was accelerated by the infiltration of rainwater during the rainfall process.

(4) Other effects, such as formation conditions, groundwater, and vegetation, had a lesser impact on ground movement in the study area.

To summarize, according to the 90-day monitoring program and the analysis of the results, the dynamic process of ground movement on Luhu slope body can be divided into stages of: mining, overburden and surface movement, surface movement in the opposite direction to the advance of the working face, surface dynamic fracture generation, surface movement in the same direction to the advance of the working face, increased length of surface dynamic fractures, local non-uniform deformation, and slope body failure.

4.3. Stability Analysis of Mining Slope

It was found that the cumulative displacement, non-uniform deformation, and special terrain conditions of the rock strata and surface affected by mining were the direct factors causing the slope body slip. In this section, the stability and risk of mining high-steep slopes was analyzed by studying the non-uniform deformation of the slope body and the change of the surface displacement field, in combination with a UAV field investigation that acquired low-altitude sequential images of the study area.

4.3.1. Non-Uniform Deformation

The non-uniform deformation of the overlying strata and surface caused by mining is often the internal factor that causes large surface cracks, uplift, caving, and even landslides. In this study, formula (9) was applied to calculate the horizontal deformation of M06–(M02, M03, M04) and M01–(M02, M03, M04). In the advancing direction of the working face, an analysis of the displacement of the monitoring points found that the movement speed at M01 was slower than that at M02, M03, and M04, which caused a stretching of the ground area. Combined with the results of a topographic analysis, it was apparent that ground movement at M02, M03, and M04 received an influence due the downhill direction of the slope body, while M01 did not, which was one of the reasons for the uneven movement

speed. The horizontal movement at M06 was in the opposite direction to that at M02, M03, and M04, resulting in an extrusion deformation dominating the area. Monitoring point M06 was located at the bottom of the slope, and its north-south slope body was limited. The amount of movement at M06 was therefore small, which resulted in the strain being concentrated in an area between M06 and (M02, M03, and M04), where the surface was raised.

$$\varepsilon(t) = 1000 \times \frac{\sqrt{(X_{t,i} - X_{t,j})^2 + (Y_{t,i} - Y_{t,j})^2 + (Z_{t,i} - Z_{t,j})^2}}{D_{0,i-j}} \text{ (mm/m)}$$

where $D_{0,i-j}$ is the distance between the monitoring points i and j at 0 days of data acquisition.

$(X_{t,i}, Y_{t,i}, Z_{t,i})$ and $(X_{t,j}, Y_{t,j}, Z_{t,j})$ are the displacements of X , Y , and Z of point i and j at moment t .

Figure 10 shows that with the continuous advancement of the working face, the extrusion deformation at M06 and (M02, M03, and M04) increased. The deformation rate of the shape of the ground surface decreased over time, with the maximum compression being more than 11 mm/m. The largest deformation occurred at M03–M06, which highlights the effect of the ground slope on the slope body. Figure 10b shows that the tensile strength of M01 and (M02, M03, and M04) increased continuously, the deformation rate decreased slowly, and the maximum deformation reached 17 mm/m. The rock formations in this area generally consist of hard rock types. When the deformation value reached 2–3 mm/m, cracks, extrusion uplift, and caving occurred on the ground. Although mining has caused large-scale deformation of the ground surface in this area, the deformation speed gradually decreased during this study. After 70 days of monitoring, the deformation rate decreased and the associated risk of high-steep slope failure decreased. The area with an increasing deformation velocity was always located in the influence zone ahead of the working face (i.e., surface non-uniform deformation was mainly concentrated in this area). However, the deformation rate and the non-uniform deformation in the influence zone behind the working face after mining began to decrease, and disturbance of the slope body decreased.

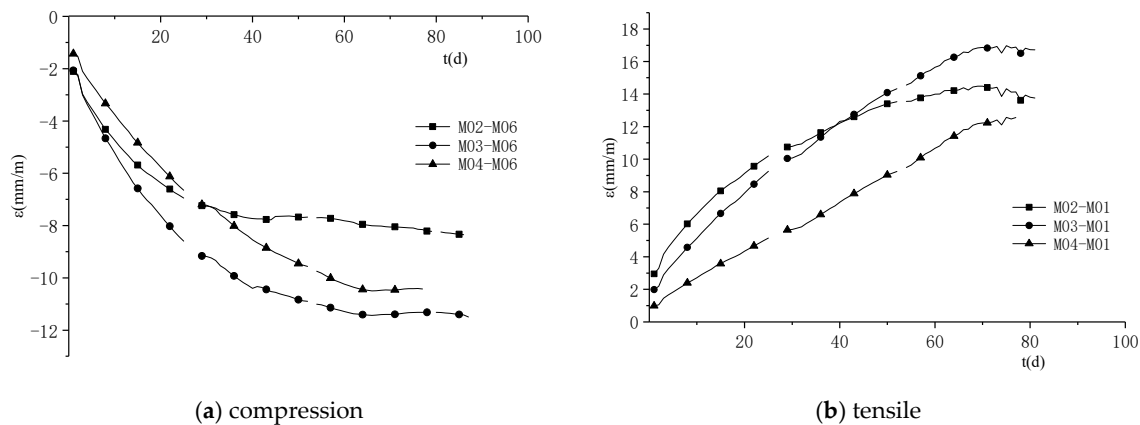


Figure 10. Non-uniform compressive and tensile deformation curves.

4.3.2. Mining Surface Displacement Field

Based on the horizontal trajectory of the monitoring points in Figure 8, the inverse distance weighted interpolation method was used to establish the displacement field near the high steep slope affected by mining, as shown in Figure 11. The stability of the high-steep slope was determined by analyzing the spatial displacement of the slope and the asynchronous movement of the area.

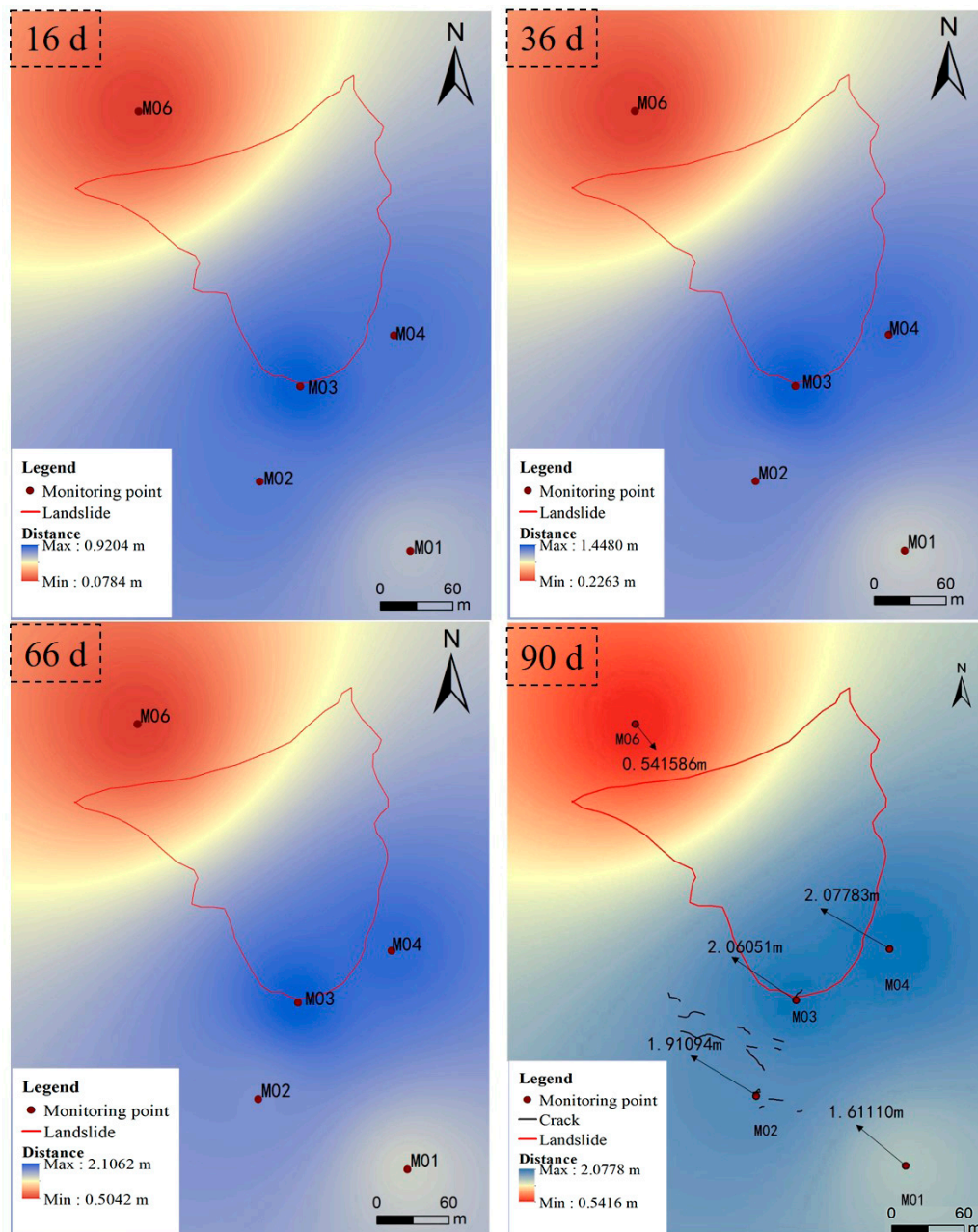


Figure 11. Displacement field of the Luhuvillage slope body.

According to the analysis shown in Figure 11, the horizontal displacement of the top slope was obviously larger than that at the foot of the slope, and the direction of movement was the opposite. The closer to the shoulder of the slope above the top of the slope, the larger the displacement (i.e., under the influence of mining the surface slope could easily cause the slope to slip), which increased the horizontal movement of the slope down to the foot. Therefore, the compression deformation of the slope foot was increased in the case of reverse horizontal movement at the foot of the slope (M06), and the deformation of the stretching area of the top of the slope was increased in the case of a small horizontal movement at M01. When the working face advanced from the back of the slope body to the front (i.e., gradually from M01 to M06), together with the influence of movement ahead and behind the working face, the surface underwent asynchronous movement. This resulted in the damage around the slope body increasing, and the sliding surface of the slope body could form easily; therefore, increasing the instability of the slope body. In the horizontal displacement field, the direction of the

plane displacement near the slope body was N45°W, which combined with the position of large cracks on the top of the slope indicated that the possibility of a landslide in that direction was more likely.

4.3.3. Ground Investigation of UAV Remote Sensing Time Series Images

Through the UAV low-altitude photogrammetry and field investigation, it was found that the main surface damage caused by mining was cracks, followed by caving. In the vicinity of the Luhu landslide, surface disasters were mainly concentrated at the top of the landslide, as shown in Figure 12a,b. In this area there were more than 10 cracks, collapse pits, and small cavings caused by surface tensile deformation, with a crack length of more than 20 m and a width of 5–50 cm, perpendicular to the slope direction. The bottom of the slope was affected by non-uniform moving compression, as shown in Figure 12d–f. The road had been uplifted by up to 1.2 m and there were several cavings identified at the foot of the slope, where more serious damage had occurred.

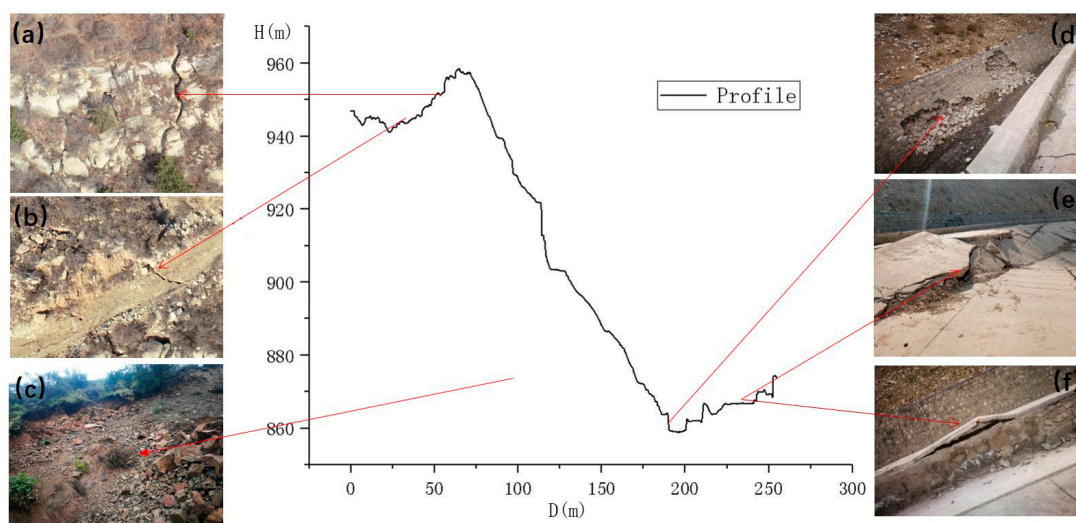


Figure 12. Landslide damage in Luhu village as a consequence of mining. (a) is near the west side of point M02; (b) is between points M01 and M02; (c) is at the foot of the slope, below point M02; (d) is at the toe of the slope body; (e,f) are located at the road of the slope foot, near the point M06.

In the area affected by mining, it was found that the number and length of surface cracks increased with the advance of the working face. Combined with the UAV time series image and the corresponding deformation degree, it was found that when $\varepsilon > 4$ mm/m (i.e., 16 d) a surface uplift deformation was produced, and when $\varepsilon > 7$ mm/m (after 36 d) a small caving was produced. As shown in Figure 13, when the deformation reached a maximum and remained constant (at the inflection point of the horizontal deformation curve), three cavings were produced near the foot of the slope. When the deformation decreased, the rate of field failure decreased.

By studying the non-uniform deformation curve, it was found that the failure of the slope body was limited, with the surface failure concentrated in areas in the accelerated or reduced stages of deformation. The instability of the slope body was increased during these periods. At the same time, the area where non-uniform deformation increased was mainly in the influence zone ahead of the working face, with the deformation rate decreasing in the influence zone behind the working face. By studying the displacement field, it was found that the horizontal movement of the top of the slope was larger than that of the foot of the slope, and they were moving in the opposite directions, which had a large influence on the stability of the slope body. From the UAV's low-altitude remote sensing time series images, it was found that with the advance of the working face, the type of ground failure in the slope area was dominated by cracks, with the number, size, and length of cracks also increasing. The high-steep slope stability in the mine was influenced by the starting deformation (low stability),

iso-accelerated deformation (increased stability), deformation deceleration (reduced stability), and deformation remaining unchanged (improved stability).

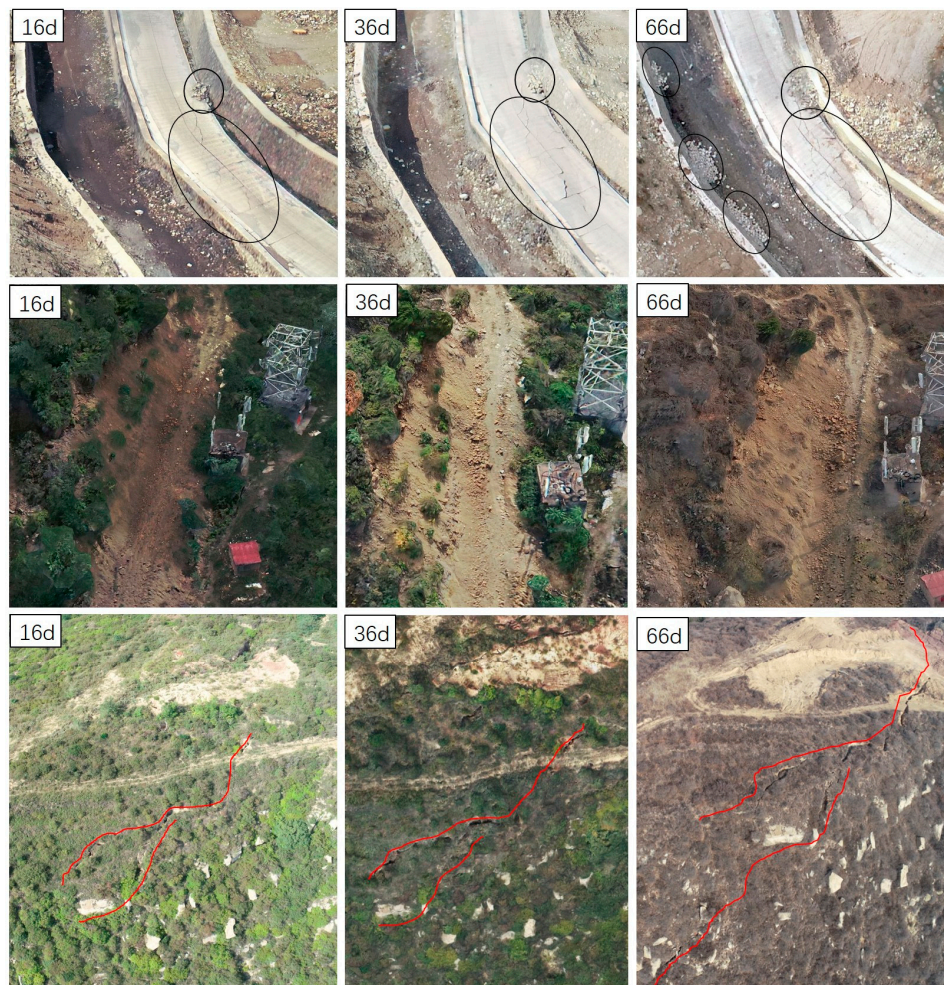


Figure 13. Unmanned Aerial Vehicle (UAV) low-altitude remote sensing time series images of Luhuvillage landslide.

5. Conclusions

(1) The GNSS monitoring system is a practical way to achieve the real-time monitoring of mining related landslides. It can provide multi-scale temporal data that can be combined with multi-source data and collaborative monitoring using other equipment, to provide reliable results.

(2) By analyzing the moving velocity at monitoring points where the overlying strata were affected by mining, the moving velocity stability threshold (i.e., the point at which the strata become active) was found to be 20 mm/d. When it was less than 20 mm/d, the strata were not normally active and had good stability. Comparing the velocity and displacement curves, it was found that continuous rainfall had a large impact on the velocity curve, but when the rainfall was lower than 15 mm, there was little effect on surface movement.

(3) Using the displacement and velocity data at the monitoring points, the response of the mining overburden, ground surface, and high-steep slopes to external factors was assessed. The overall impact could be considered a consequence of mining, terrain conditions, rainfall, and other factors. It was found that mining was the main external force driving slope body deformation, while the topographic conditions had a large influence on the displacement of the slope body in a certain direction, providing

sufficient conditions for a slope body slip. Rainfall has a staged effect on the slope body, and accelerated the formation of a sliding surface.

(4) Non-uniform deformation and terrain conditions caused by mining were the direct causes of slope body instability. A field investigation of non-uniform deformation, displacement fields, and UAV low-altitude remote sensing time series images showed that the stability of the slope body was low when the deformation rate changed suddenly due to mining, and the stability of the slope body was high when the deformation was uniform or when no deformation occurred. It was found that the non-uniform and asynchronous deformation was mainly concentrated in the influence zone ahead of the working face, and the hysteretic influence zone behind the working face was the main area of surface subsidence.

Author Contributions: Conceptualization, X.L. (Xugang Lian); methodology, X.L. (Xugang Lian), H.H. and Y.C.; software, H.Y.; validation, Z.L.; formal analysis, H.H. and Y.C.; investigation, X.L. (Xugang Lian) and Z.L.; resources, Z.L.; data curation, X.L. (Xugang Lian), Z.L. and H.Y.; writing—original draft preparation, Z.L. and H.Y.; writing—review and editing, X.L. (Xugang Lian); visualization, X.L. (Xiaoyu Liu); supervision, X.L. (Xugang Lian); project administration, X.L. (Xugang Lian); funding acquisition, X.L. (Xugang Lian) All authors have read and agreed to the published version of the manuscript.

Funding: This research was funded by [National Natural Science Foundation of China] grant number [51704205], [Shanxi Natural Science Foundation of China] grant number [201701D221025], and [Key R&D Plan projects in Shanxi Province of China] grant number [201803D31044]. The APC was funded by [51704205].

Conflicts of Interest: The authors declare no conflicts of interest.

References

- Li, Y.R. A review of shear and tensile strengths of the Malan Loess in China. *J. Eng. Geol.* **2018**. [[CrossRef](#)]
- Free, M.; Rossetto, T.; Peiris, N.; Taucer, F.; Zhao, B.; Koo, R.; Wang, J.; Ma, X.; Verrucci, E. The wenchuan china earthquake of may 12, 2008: A preliminary field report by eefit. 2008. In Proceedings of the 14th World Conference on Earthquake Engineering, Beijing, China, 12–17 October 2018.
- Ma, J.; Tang, H.; Liu, X.; Wen, T.; Zhang, J.; Tan, Q.; Fan, Z. Probabilistic forecasting of landslide displacement accounting for epistemic uncertainty: A case study in the three gorges reservoir area, china. *Landslides* **2018**, *15*, 1145–11453. [[CrossRef](#)]
- Chen, W.; Li, X.; Wang, Y.; Chen, G.; Liu, S. Forested landslide detection using lidar data and the random forest algorithm: A case study of the three gorges, china. *Remote Sens. Environ.* **2014**, *152*, 291–301. [[CrossRef](#)]
- Mantovani, F.; Soeters, R.; Van Westen, C.J. Remote sensing techniques for landslide studies and hazard zonation in europe. *Geomorphology* **1996**, *15*, 213–225. [[CrossRef](#)]
- Li, Z.H.; Song, C.; Yu, C.; Xiao, R.Y.; Chen, L.F.; Luo, H.; Dai, K.R.; Ge, D.Q.; Ding, Y.; Zhang, Y.X.; et al. Application of Satellite Radar Remote Sensing to Landslide Detection and Monitoring: Challenges and Solutions. *Geomatics Inf. Sci. Wuhan Univ.* **2019**, *44*, 967–979.
- Yan, G.; Yin, Y.; Huang, B.; Zhang, Z.; Zhu, S. Formation mechanism and deformation characteristics of Jinjiling landslide in Wushan, Three Gorges Reservoir region. *Landslides* **2019**, *16*, 2087–2101. [[CrossRef](#)]
- Zhao, H.J.; Ma, F.S.; Guo, J.; Wu, Z.Q.; Zhang, Y.L. Effect of open-pit to underground mining on slope stability in Longshou Mine. *J. China Coal Soc.* **2011**, *36*, 1635–1641.
- Gao, W.; Dai, S.; Chen, X. Landslide prediction based on a combination intelligent method using the GM and ENN: Two cases of landslides in the Three Gorges Reservoir, China. *Landslides* **2019**. [[CrossRef](#)]
- Hungchou, L.I.N.; Yuzhen, Y.U.; Guangxin, L.I.; Hua, Y.A.N.G.; Jianbing, P.E.N.G. A Simplified Numerical Approach for the Prediction of Rainfall-Induced Retrogressive Landslides. *Acta Geol. Sin. (Engl. Ed.)* **2016**, *41*, 1471–1480. [[CrossRef](#)]
- Zakharov, V.N.; Malinnikova, O.N.; Trofimov, V.A.; Filippov, Y.A. Stability and creeping of landslide slope. *J. Min. Sci.* **2014**, *50*, 1007–1016. [[CrossRef](#)]
- Cascini, L.; Cuomo, S.; Della Sala, M. Spatial and temporal occurrence of rainfall-induced shallow landslides of flow type: A case of sarno-quindici, italy. *Geomorphology* **2011**, *126*, 148–158. [[CrossRef](#)]
- Efremidis, G.; Avlonitis, M.; Konstantinidis, A.; Aifantis, E.C. A statistical study of precursor activity in earthquake-induced landslides. *Comput. Geotech.* **2017**, *81*, 137–142. [[CrossRef](#)]

14. Zhu, C.; Zhang, J.; Liu, Y.; Ma, D.; Li, M.; Xiang, B. Comparison of GA-BP and PSO-BP neural network models with initial BP model for rainfall-induced landslides risk assessment in regional scale: A case study in Sichuan, China. *Nat. Hazards*. **2019**. [[CrossRef](#)]
15. Liu, J.; Li, S.L.; Chen, T. Landslide Susceptibility Assessment Based on Optimized Random Forest Model. *Geomat. Inf. Sci. Wuhan Univ.* **2018**, *43*, 1085–1091.
16. Chen, G.Q.; Huang, R.Q.; Shi, Y.C.; Xu, Q. Stability analysis of slope based on dynamic and whole strength reduction methods. *Chin. J. Rock Mech. Eng.* **2014**, *33*, 243–256.
17. Martín, A.; Anquela, A.B.; Dimas-Pagés, A.; Cos-Gayón, F. Validation of performance of real-time kinematic ppp. a possible tool for deformation monitoring. *Measurement* **2015**, *69*, 95–108. [[CrossRef](#)]
18. Komac, M.; Holley, R.; Mahapatra, P.; van der Marel, H.; Bavec, M. Coupling of gps/gnss and radar interferometric data for a 3d surface displacement monitoring of landslides. *Landslides* **2014**, *12*, 241–257. [[CrossRef](#)]
19. Mochizuki, K.; Mitsui, Y. Crustal deformation model of the Beppu–Shimabara graben area, central Kyushu, Japan, based on inversion of three-component GNSS data in 2000–2010. *Earth Planets Space* **2016**, *68*, 177. [[CrossRef](#)]
20. Barut, R.A.; Trinder, J.; Rizos, C. Analysing Post-Seismic Deformation Of Izmit Earthquake With Insar, Gnss And Coulomb Stress Modelling. *Int. Arch. Photogramm. Remote Sens. Spat. Inf. Sci.* **2016**, *41*, 417–421. [[CrossRef](#)]
21. Jianshaneg, Y.U.; Bin, Z.H.A.O.; Kai, T.A.N.; Dongzhen, W.A.N.G. Analysis of GNSS Postseismic Deformation of Wenchuan Earthquake. *Acta Geodaet. Cartogr. Sin.* **2018**, *47*, 1196–1206.
22. Wang, Y.; Gan, W.; Chen, W.; You, X.; Lian, W. Coseismic displacements of the 2017 Jiuzhaigou M7.0 earthquake observed by GNSS: Preliminary results(Article). *Acta Geophys. Sin.* **2018**, *61*, 161–170. [[CrossRef](#)]
23. Guirong, L.; Xiaoqiang, W.; Jie, L.; Daiqin, L.; Yushan, A.; Li, C.; Rui, L. Research on Regional Crustal Deformation Characteristics Using Displacement Time Series Data of GNSS Reference Stations in Xinjiang. *Earthq. Res. China* **2018**, *32*, 388–399.
24. Mendoza, L.; Richter, A.; Fritsche, M.; Hormaechea, J.L.; Perdomo, R.; Dietrich, R. Block modeling of crustal deformation in tierra del fuego from gnss velocities. *Tectonophysics* **2015**, *651–652*, 58–65. [[CrossRef](#)]
25. Ishchenko, M. Investigation of Deformations of the Earth Crust on the Territory of Ukraine Using a GNSS Observations. *Artif. Satell.* **2018**, *53*, 117–126. [[CrossRef](#)]
26. Nishimura, T.; Takada, Y. San-in shear zone in southwest Japan, revealed by GNSS observations. *Earth Planets Space* **2017**, *69*, 85. [[CrossRef](#)]
27. Richter, A.; Ivins, E.; Lange, H.; Mendoza, L.; Schröder, L.; Hormaechea, J.L.; Casassa, G.; Marderwald, E.; Fritsche, M.; Perdomo, R.; et al. Crustal deformation across the Southern Patagonian Icefield observed by GNSS. *Earth Planet. Sci. Lett.* **2016**, *452*, 206–215. [[CrossRef](#)]
28. Fujita, M.; Nishimura, T.; Miyazaki, S. Detection of small crustal deformation caused by slow slip events in southwest Japan using GNSS and tremor data(Article). *Earth Planets Space* **2019**, *71*. [[CrossRef](#)]
29. Ma, F.X.; Xi, R.J.; Xu, N. Analysis of railway subgrade frost heave deformation based on GPS. *Geod. Geodyn.* **2016**, *7*, 143–147. [[CrossRef](#)]
30. Luo, L.H.; Ma, W.; Zhuang, Y.L.; Zhang, Z.Q. Deformation monitoring and analysis at two frost mounds during freeze–thaw cycles along the Qinghai–Tibet Engineering Corridor. *Sci. Cold Arid Reg.* **2017**, *9*, 378–383.
31. Lee, S.-W.; Yun, S.-H.; Kim, D.H.; Lee, D.; Lee, Y.J.; Schutz, B.E. Real-time volcano monitoring using GNSS single-frequency receivers(Article). *J. Geophys. Res. Solid Earth* **2015**, *120*, 8551–8569. [[CrossRef](#)]
32. Riccardi, U.; Arnosó, J.; Benavent, M.; Vélez, E.; Tamarro, U.; Montesinos, F.G. Exploring deformation scenarios in Timanfaya volcanic area (Lanzarote, Canary Islands) from GNSS and ground based geodetic observations(Article). *J. Volcanol. Geotherm. Res.* **2018**, *357*, 14–24. [[CrossRef](#)]
33. Tao, T.Y.; Liu, J.B.; Qu, X.C.; Gao, F. Real-time monitoring rapid ground subsidence using GNSS and Vondrak filter. *Acta Geophys.* **2019**, *67*, 133–140. [[CrossRef](#)]
34. Wang, D.H.; Meng, X.L.; Gao, C.F.; Pan, S.G.; Chen, Q.S. Multipath extraction and mitigation for bridge deformation monitoring using a single-difference model. *Adv. Space Res.* **2017**, *60*, 2882–2895. [[CrossRef](#)]
35. Chen, Q.; Jiang, W.; Meng, X.; Jiang, P.; Wang, K.; Xie, Y.; Ye, J. Vertical deformation monitoring of the suspension bridge tower using GNSS: A case study of the Forth Road Bridge in the UK(Article). *Remote Sens.* **2018**, *10*, 364. [[CrossRef](#)]
36. Barzaghi, R.; Cazzaniga, N.E.; De Gaetani, C.I.; Pinto, L.; Tornatore, V. Estimating and Comparing Dam Deformation Using Classical and GNSS Techniques. *Sensors* **2018**, *18*, 756. [[CrossRef](#)]

37. Yavaşoğlu, H.H.; Kalkan, Y.; Tiryakioğlu, İ.; Yigit, C.O.; Özbey, V.; Alkan, M.N.; Bilgi, S.; Alkan, R.M. Monitoring the deformation and strain analysis on the Ataturk Dam, Turkey. *Geomat. Nat. Hazards Risk* **2018**, *9*, 94–107. [[CrossRef](#)]
38. Huang, G.; Du, Y.; Meng, L.; Huang, G.; Wang, J.; Han, J. Application Performance Analysis of Three GNSS Precise Positioning Technology in Landslide Monitoring. *Lect. Notes Electr. Eng.* **2017**, *437*, 137–148.



© 2020 by the authors. Licensee MDPI, Basel, Switzerland. This article is an open access article distributed under the terms and conditions of the Creative Commons Attribution (CC BY) license (<http://creativecommons.org/licenses/by/4.0/>).